Available online at www.sciencedirect.com

jmr&t Journal of Materials Research and Technology

www.jmrt.com.br

Original Article

Study of the tensile behavior of AISI type 316 stainless steel using acoustic emission and infrared thermography techniques

Thodamrakandy Haneef, Barid Baran Lahiri, Subramaniam Bagavathiappan, Chandan Kumar Mukhopadhyay, John Philip, Bhagi Purna Chandra Rao, Tamanna Jayakumar*

Non Destructive Evaluation Division, Metallurgy and Materials Group, Indira Gandhi Center for Atomic Research, Kalpakkam, India

ARTICLE INFO

Article history:
Received 20 June 2014
Accepted 15 December 2014
Available online 15 January 2015

Keywords:
Tensile testing
AISI type 316 stainless steel
Acoustic emission and infrared thermography

ABSTRACT

Acoustic emission (AE) and infrared thermography technique (IRT) have been used to study the tensile behavior of AISI type 316 stainless steel. Strain rates of tensile testing were varied from $1.4 \times 10^{-3}\ s^{-1}$ to $1.4 \times 10^{-2}\ s^{-1}$. AE root mean square voltage increases with increase in strain rate due to the increase in source activation. Dominant frequency of the AE signals generated during different regions of tensile deformation has also been used to compare the results for different strain rates. The dominant frequency increases from elastic region to around 590 kHz during work hardening and 710 kHz around ultimate tensile strength (UTS) for all the strain rates. Temperature changes during different regions of deformation are monitored using infrared thermography. The temperature rise in the work hardening region is found to approximately increase linearly with time and from the slopes of the linear regression analyses the rate of temperature rise in the work-hardening region is obtained which is found to be very sensitive to strain rates. From the experimental results an empirical equation that relates the rate of temperature increase with strain rate and thermal hardening coefficient is obtained. The correlation between the variation of AE dominant frequency and temperature rise during different deformation regions provided better insight into the tensile behavior of AISI type 316 SS for different strain rates.

1. Introduction

Acoustic emission and infrared thermography are potential nondestructive evaluation (NDE) techniques and they can be effectively used for structural integrity monitoring applications and characterizing damages in materials [1–3]. AE is defined as the class of phenomenon whereby transient elastic waves are generated by rapid release of energy from

* *Corresponding author.*
E-mail: ckm@igcar.gov.in (C.K. Mukhopadhyay).
http://dx.doi.org/10.1016/j.jmrt.2014.12.008

localized sources in a material [4]. Many of the deformation related microscopic processes involve some stress relaxation. Monitoring acoustic emission from a deforming material can give significant information about the microscopic mechanisms involved, because magnitude of this stress relaxation is dependent upon the particular process.

Acoustic emission during tensile deformation depends on various microstructural features including grain size, carbon content, cooling rate, etc. Investigations carried out indicate that higher grain size of a material usually leads to higher AE generation and explained by changes in slip increment accompanying changes in grain size [5,6]. Wadley and Scruby [7] investigated the AE generated during tensile deformation of low alloy steels with carbon content varying between 0.06 and 0.49 wt.% and as a function of cooling rate. It was reported that specimens with (a) slowly cooled microstructures (with $\geq$10 μm ferrite dimension), (b) low initial dislocation density and (c) very widely spaced precipitates, generate highest AE activity. This was attributed to higher glide distance and higher velocity of dislocations in the ferrite phase [7]. Carpenter and Pfleiderer [8] reported that the magnitude of the peak rms voltage at yield increases with increasing yield strength in AISI 4340 steel, tempered at different conditions. This was attributed to the increase in difficulty in initiating and propagating Luder's band with increasing strength levels [8].

AE technique has been effectively used to study the micro-mechanistic aspects of tensile deformation and fracture behavior in different materials [9–11]. These studies have shown that dislocation kinetics, dynamic strain aging and fracture/decohesion of inclusions give rise to specific characteristic AE signals. Khamedi et al. [9] studied the effect of volume fractions of martensite on the AE behavior of dual phase steel under tensile loading. AE dominant frequency was used to find different failure modes i.e. ferrite–martensite interface decohesion or martensite phase fracture. Haneef et al. [10] studied the effect of heat treatment on the Lüders band formation in medium carbon steel using acoustic emission technique. Characteristic dominant AE frequencies are observed during Luders deformation of water quenched and tempered specimens of medium carbon steel [10]. AET has been used to monitor low temperature tensile deformation of AISI type 304LN stainless steel and a mechanism based model is proposed from cumulative AE counts for evolution of martensite during low temperature test [11]. AE during tensile deformation and fracture of AISI type 316 stainless steel was studied [12,13]. In commercial grade 316 stainless steel, burst type AE signals occur due to decohesion and/or fracture of inclusions [12,13], whereas in nuclear grade 316 stainless steel, AE is mainly generated by dislocation activity. As compared to ambient temperature, deformation at higher temperatures (473–973 K) results in higher AE generation in 316 stainless steel and this is due to serrated flow by the occurrence of dynamic strain ageing [12]. The uniqueness of AE technique for characterization of various deformation processes such as particle shearing, Orowan looping and decohesion of carbides, during the tensile deformation of a nickel base superalloy Nimonic PE16, was also shown [12].

Studies have been carried out to find the influence of extent of plastic deformation on the frequency of AE signals generated during tensile deformation [12,14]. These studies indicated that the predominant frequency of the AE signal linearly increases from 0.475 to 0.66 MHz with increase in plastic strain from 2% to onset of necking in 316 stainless steel. AET has been used to detect the micro plastic yielding occurring during macroscopic plastic deformation in 316 stainless steel [15]. The approximate frequency range of AE signals generated from dislocation sources operating during pre-yield and near-yield tensile deformation in this steel was predicted [15]. For 316 stainless steel with grain size of 45 μm and tested at a strain rate of $5.2 \times 10^{-4}\,s^{-1}$, the expected frequency of AE corresponding to the generation of Frank-Reed and grain-boundary sources during yielding was theoretically predicted to be 133 kHz and experimentally verified as 170 kHz [15].

Many studies have been reported on AE during tensile deformation of different materials for different strain rates [16–18]. Pattnaik et al. [16] have shown that AE signal generated during deformation of α-brass is strain rate sensitive and intensity of the AE signals increases with strain rate. They have attributed the increase in intensity of AE with increase in strain rate to dislocation motion and twinning. Zhiyuan et al. [17] studied the effect of strain rate on AE during deformation of discontinuous yielding materials and have successfully classified different deformation stages with the help of AE waveforms. AET was also used to study the effect of strain rate on tensile deformation of 316 stainless steel [18]. Increase in AE generation with increase in strain rate was attributed to increase in the activation of AE sources during tensile deformation [18].

Infrared thermography is a non-contact temperature measurement methodology where the infrared radiations emitted by an object is recorded using an infrared camera and the temperature of the object is measured from the intensity of the infrared radiations using Stefan–Boltzmann's law, which is described below.

$$\frac{q}{A} = \sigma \varepsilon T^4 \tag{1}$$

Here, q is the rate of energy emission (W), A is the area of the emitting surface (m^2), σ is the Stefan–Boltzmann's constant ($\sigma = 5.676 \times 10^{-8}\,Wm^{-2}\,K^{-4}$) and ε is the emissivity of the surface. For a perfect black-body, $\varepsilon = 1$ and for real surfaces, $\varepsilon < 1$. Detailed discussion on various IRT based experimental techniques and data analysis procedures can be found elsewhere [19]. IRT is routinely used for non-destructive evaluation of metallic and composite specimens [20,21], detection of weld defects [22] and condition monitoring applications [2].

AISI type 316 austenitic stainless steel is an important structural material for fast breeder reactor applications. Venkataraman et al. [18] used acoustic emission and infrared thermography (IRT) techniques simultaneously to study the effect of strain rate on tensile deformation of 316 stainless steel. The techniques were selected based on the fact that dissipated energy during tensile deformation has both heat energy and elastic wave energy components. However, this study was based on time domain analysis of AE signals and the AE count rate was correlated with the strain rate. The objective of the present study is to use AE frequency analysis to characterize the sources of AE during tensile deformation of 316 stainless steel. Compared to time domain, frequency domain

analysis of AE has an advantage since the dominant frequency present in the frequency spectrum should be inversely proportional to the duration of the dynamic event. This can provide information on the time scale of the AE process and can thus be used to characterize the evolution of dynamic source event [14]. Moreover, an attempt has been made to correlate AE dominant frequency generated during different deformation regions with temperature rise, measured using IRT, for various strain rates. A new empirical relation between the rate of temperature increase and strain rate is proposed. Another objective is to show the complementary nature of these two NDE techniques for their effective use for online characterization of deformation processes.

2. Experimental

The chemical composition of AISI 316 type stainless steel used to prepare tensile specimens is as follows (in wt.%): Cr/17.1, Ni/12.1, Mn/1.66, Mo/2.4, C/0.04, Si/0.67, Co/0.27,Cu/0.10, and Fe/Balance. Flat tensile specimens having gauge dimensions of 30 mm × 6 mm × 5 mm were solution annealed at 1323 K for 30 min. These specimens were subjected to tensile deformation at strain rates $1.4 \times 10^{-3}\,s^{-1}$, $2.8 \times 10^{-3}\,s^{-1}$, $6.9 \times 10^{-3}\,s^{-1}$ and $1.4 \times 10^{-2}\,s^{-1}$ at ambient temperature (~298 K).

Acoustic emission signals generated during tensile deformation were recorded using AE DiSP system supplied by Physical Acoustic Corporation, USA. Schematic of the experimental setup used is shown in Fig. 1. A piezoelectric sensor having resonant frequency at 150 kHz, a preamplifier with 40 dB gain and a band pass filter (100–300 kHz) were used to record the AE signals. The total gain and threshold were maintained at 80 and 37 dB, respectively. In order to study the frequency characteristics of AE signal, a broadband piezoelectric sensor (100 kHz–1 MHz) was used. The sensors were fixed at shoulder to gauge transition regions of the specimens using silicon grease as couplant. The gain and threshold were so selected that no external noise was recorded during the test [23]. The AE signals were digitized at a sampling rate of 5 Mega samples per second.

Infrared thermography measurements were performed using FLIR SC 5000 infrared camera. The camera has indium antimonide (InSb) focal plane array (320 × 256) detector. The spectral range of the camera is 2.0–5.1 μm. The detector elements are cooled using a Stirling cycle and the thermal sensitivity of the camera is better than 25 mK (i.e. NETD < 0.025 K, where NETD is noise equivalent temperature difference). For avoiding viewing angle effects, the camera was oriented in such a way that the camera axis is perpendicular to the specimen surface. The camera to specimen distance was maintained at 500 mm for all the cases. Thermal images were continuously acquired at 25 frames per second during tensile deformation and digitally stored in a personal computer. The acquired images were later analyzed using Altair software. The tensile specimens were black painted for enhancing the surface emissivity. Constant ambient temperature was maintained during the experiments. During analysis of the acquired infrared images, a region of interest was selected for each frame and the average temperature of the pixels in the region was used for further analysis. This technique essentially reduces the experimental variations as temperature is measured over a large number of pixels simultaneously in real time and the average temperature is also computed in real time using Altair software [24,25].

3. Results and discussion

3.1. *Acoustic emission*

Variation of nominal stress and AE root mean square (RMS) voltage with nominal strain for different strain rates, viz. 1.4×10^{-3}, 2.8×10^{-3}, 6.9×10^{-3} and $1.4 \times 10^{-2}\,s^{-1}$ is shown in Fig. 2. It is seen that dominant AE is generated in the region before and during yielding, and during initial region of work hardening. AE generated then reduced with increasing nominal strain. Higher AE activity is observed again when final fracture occurred. These observations are consistent with the reported results in austenitic stainless steels [12,13,18,23].

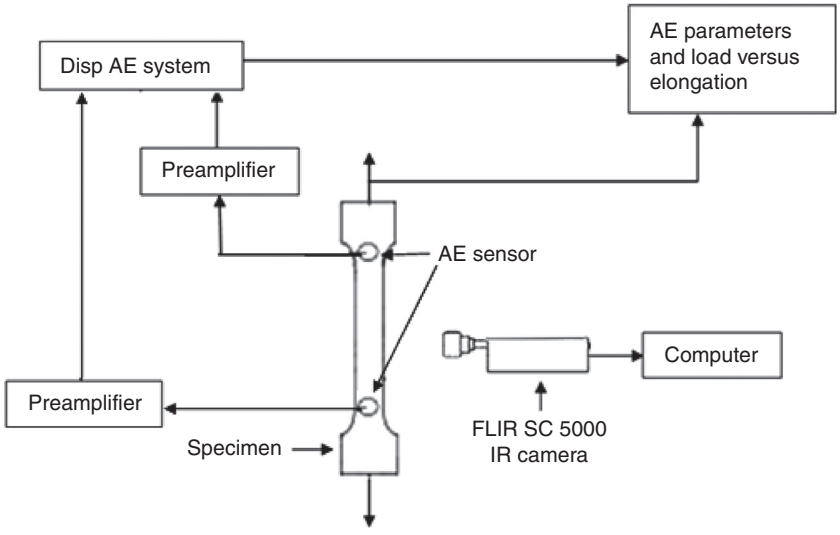

Fig. 1 – Schematic of the experimental set up.

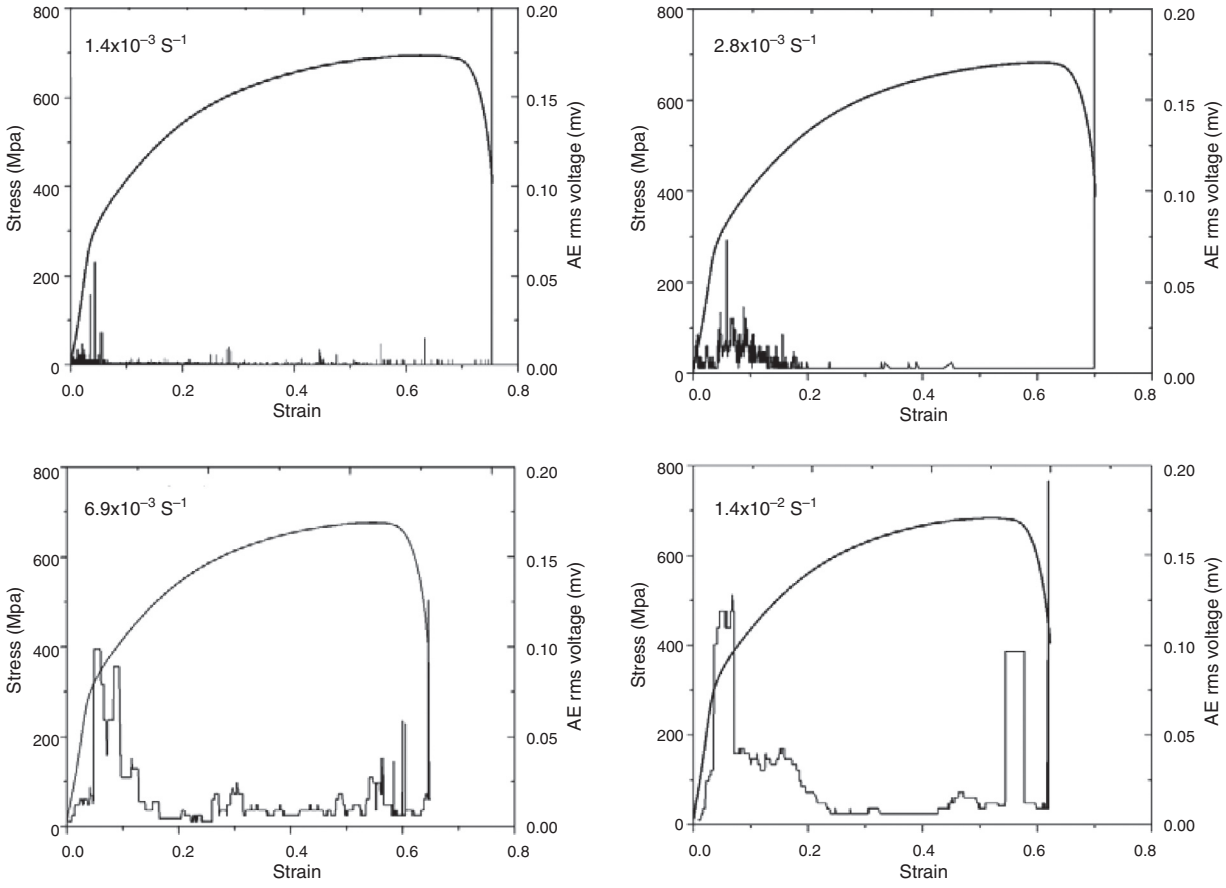

Fig. 2 – Variation of nominal stress and AE *rms* voltage with nominal strain for different strain rates.

The extent of acoustic activity generated during deformation of a material depends on a number of factors such as type of material and its metallurgical history, level of plastic strain and presence of any inclusions or second phase. AE generated during tensile deformation of metallic materials indicated that for materials having a single-phase microstructure, a peak in AE occurs at initial strain levels corresponding to the phenomenon of macroyielding [26,27]. The AE results obtained in this investigation for different strain rates are in agreement with the normally observed AE activity during tensile deformation of metallic materials having essentially a single-phase microstructure. It is also known that in nuclear grade stainless steel, AE is mainly generated by dislocation activity [12]. AE generated during deformation decreases with increase in strain and this is due to decrease in the glide distance for moving dislocations and the reduced rate of formation of dislocation avalanche [12].

It can be seen from Fig. 2 that the AE generated during different deformation regions increases with increase in strain rate. This is due to the increase in source activation with increase in the strain rate. These results are in agreement with the results reported earlier for 316 stainless steel [14,18]. Increase in AE generation with increasing strain rate is also in agreement with the results in α-brass [16], where AE is generated by both dislocation motion and twinning. It is also seen from Fig. 2 that the graphs for the strain rates $6.9 \times 10^{-3}\,s^{-1}$ and $1.4 \times 10^{-2}\,s^{-1}$ show a peak on the final part of the AE curve as compared to the graphs of the lower strain rates. This is due to higher AE RMS voltage before final fracture and can be seen just after necking. The occurrence of high AE peak after necking is due to faster crack propagation and faster fracture process in higher strain rate tests as compared to the tests at lower strain rates.

Frequency spectrum of AE signals corresponding to different regions of tensile deformation i.e. region-1 (0–3% nominal strain covering elastic region), region-2 (3–10% nominal strain covering the yield region), region-3 (10–20% nominal strain), region-4 (around UTS) and region-5 (UTS to before final fracture covering the necking) have been used for further analysis. In each region, ten AE waveforms have been analyzed. Figs. 3 and 4 show one set of frequency spectrum of AE waveforms generated for strain rates 1.4×10^{-3} and $1.4 \times 10^{-2}\,s^{-1}$ respectively for (a) region-1, (b) region-2, (c) region-3 (d) region-4 and (e) region-5. The average values of the dominant frequencies of AE signals for these regions for four different strain rates are shown in Table 1a–d. The values of standard deviation and 95% confidence interval associated with the average values of the dominant frequency for different strain rates are also shown in Table 1a–d.

The dominant AE was reported in frequency spectrum analysis of AE signal obtained during tensile deformation of 316 stainless steel [12]. Dominant AE is determined from frequency amplitude plot (frequency spectrum) and it is the maximum amplitude peak in the frequency spectrum. In

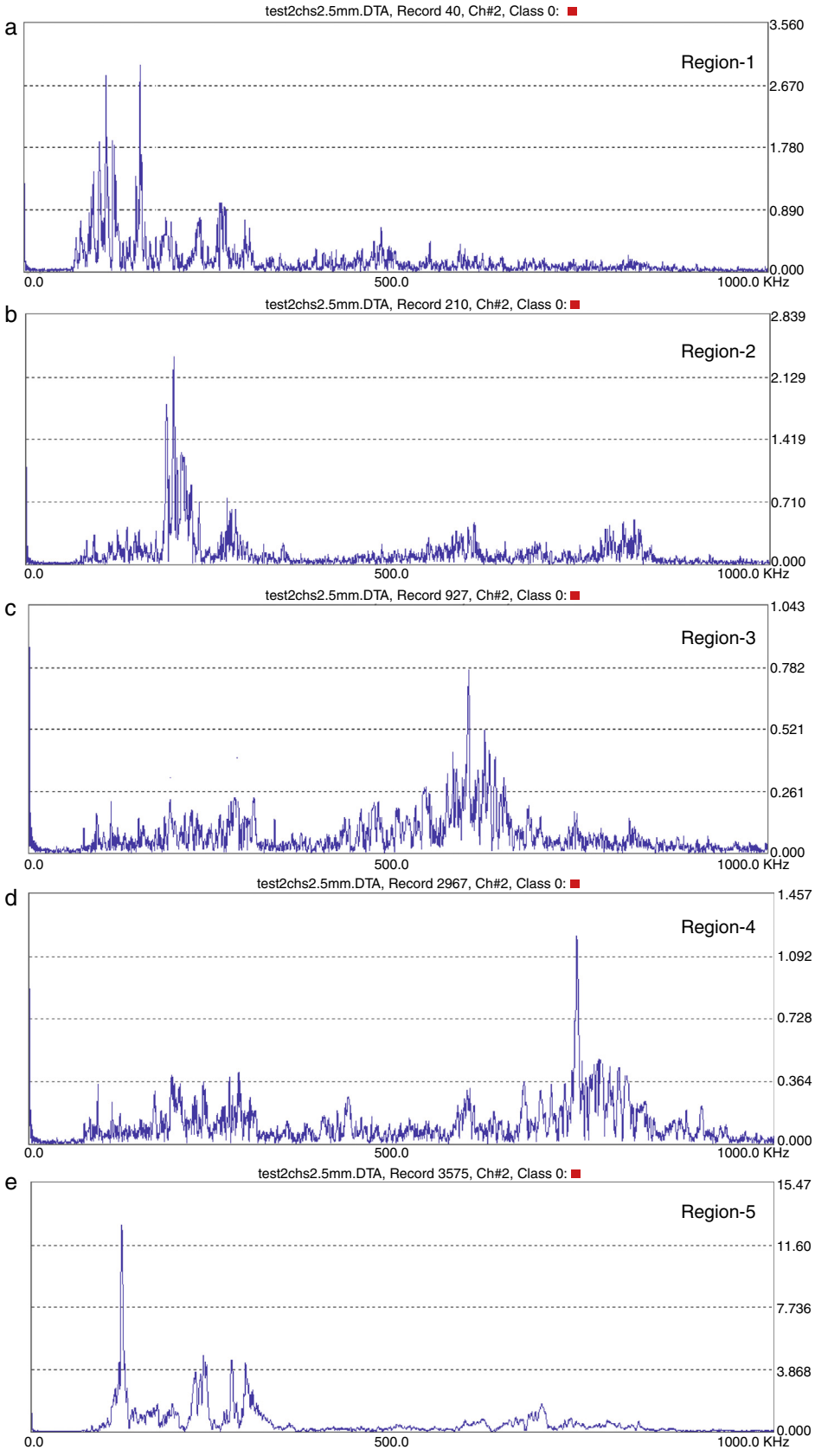

Fig. 3 – AE dominant frequency generated during different regions of deformation for 1.4×10^{-3} s^{-1} strain rate test for (a) region-1, (b) region-2, (c) region-3, (d) region-4 and (e) region-5.

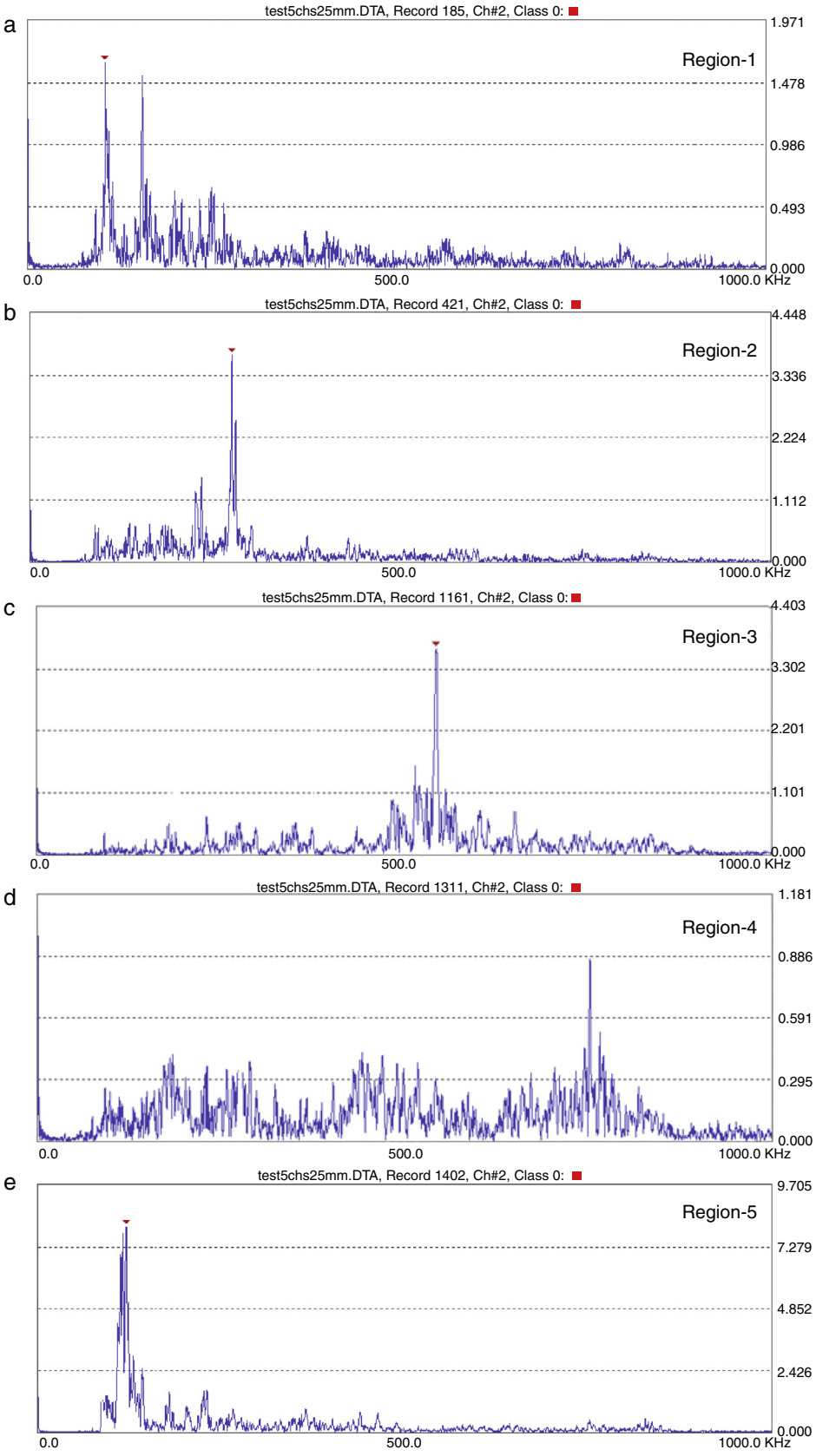

Fig. 4 – AE dominant frequency generated during different regions of deformation for $1.4 \times 10^{-2}\ s^{-1}$ strain rate test for (a) region-1, (b) region-2, (c) region-3, (d) region-4 and (e) region-5.

Table 1 – AE dominant frequency generated during different regions of deformation for different strain rates.

(a)

	Strain rate 1.4×10^{-3}					
	Region-1		Region-2	Region-3	Region-4	Region-5
	Peak-1	Peak-2				
Mean	120	150	190	590	713	130
Sd	5	5	5	11	12	5
CIL	114	144	184	579	701	124
CIU	126	156	196	601	726	136

(b)

	Strain rate 2.8×10^{-3}					
	Region-1		Region-2	Region-3	Region-4	Region-5
	Peak-1	Peak-2				
Mean	110	144	200	580	730	120
Sd	9	5	10	12	14	10
CIL	98	138	188	565	712	108
CIU	122	151	212	595	748	132

(c)

	Strain rate 6.9×10^{-3}					
	Region-1		Region-2	Region-3	Region-4	Region-5
	Peak-1	Peak-2				
Mean	110	140	240	580	710	110
Sd	7	10	10	10	16	12
CIL	101	128	228	568	690	95
CIU	119	152	252	592	730	125

(d)

	Strain rate 1.4×10^{-2}					
	Region-1		Region-2	Region-3	Region-4	Region-5
	Peak-1	Peak-2				
Mean	120	150	270	590	720	120
Sd	10	10	14	20	22	7
CIL	108	138	252	565	692	111
CIU	132	162	288	615	748	129

Sd, Standard deviation, CIL, 95% lower confidence limit, CIU, 95% upper confidence limit.

Figs. 3 and 4, dominant frequencies are related to absolute peaks (maximum amplitudes). In region-1 of Figs. 3 and 4, two peaks with almost same amplitude were observed and hence both are regarded as two dominant frequencies. The dominant frequency can provide information on the time scale (duration) of AE source and two dominant frequencies present in Fig. 3 (120 and 150 kHz) for region-1 show that duration of dynamic source event is different. Figs. 3 and 4 also show some minor peaks. These are attributed to the material itself. For AE frequency analysis, wide band AE sensor with range (100 kHz–1 MHz) has been used and it is sensitive to entire frequency range and hence small peaks are observed along with dominant frequency peak.

It is seen that, in region-1, signals are generated at two dominant frequencies, which are almost similar for different strain rates. This observation reveals that AE source mechanism in this region is not varying with strain rate. The predominant frequency increases with increasing strain up to UTS and then decreases. With increase in strain, single dominant frequency is observed for region-2 (190 kHz), region-3 (590 kHz) and region-4 (713 kHz) for $1.4 \times 10^{-3}\,s^{-1}$ strain rate. The values are at 200, 580 and 730 kHz for region-1, region-2 and region-3 respectively for the strain rate of $2.8 \times 10^{-3}\,s^{-1}$. The values are at 240, 580 and 710 kHz for different regions for the strain rate of $6.9 \times 10^{-3}\,s^{1}$. The values are at 270, 590 and 720 kHz for different regions for the strain rate $1.4 \times 10^{-2}\,s^{-1}$. In the necking region, a lower dominant frequency (110–130 kHz) is observed as compared to earlier regions for all the strain rates.

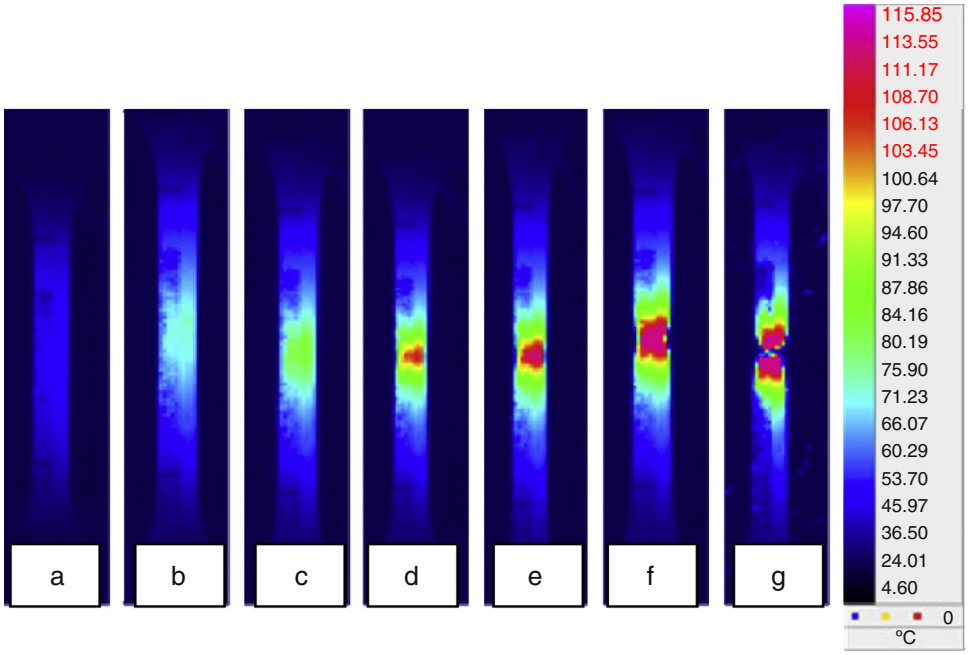

Fig. 5 – Thermal images obtained during tensile deformation at a strain rate of $1.4 \times 10^{-2}\ s^{-1}$. (a) 20%, (b) 50%, (c) 54%, (d) 56%, (e) 58%, (f) 59% and (g) 61% nominal strain.

The approximate frequency range of AE signals generated during pre-yield and near-yield tensile deformation in 316 stainless steel tested at a strain rate of $5.2 \times 10^{-4}\ s^{-1}$ is 133 kHz theoretically and 170 kHz experimentally [15]. The frequency of the AE signals obtained in region 1 in the present investigation is thus in agreement with the earlier observed results in 316 stainless steel. Shift in the dominant frequency to higher frequency up to UTS region can be explained based on mean free path of dislocations. Raj et al. [14] reported that the dominant frequency in AE spectrum is inversely proportional to event duration of the dynamic event generating the AE signal. Mean event duration of AE signal is proportional to the mean free path of dislocations generated and the mean free path decreases when a material is work hardened. Decrease in mean free path of dislocations between obstacles is responsible for shift in the AE frequency to higher values with deformation.

It is seen from Table 1 that the dominant frequency of AE in region 2 increases with strain rate and the values are 190, 200, 240 and 270 kHz for strain rate 1.4×10^{-3}, 2.8×10^{-3}, 6.9×10^{-3} and $1.4 \times 10^{-3}\ s^{-1}$ respectively. Shift in dominant frequency to higher value with increase in strain rate can be explained based on the velocity of dislocations (v), which are generated during region 2. The proportionality between v and strain rate ($\dot{\varepsilon}$) is observed during yielding in different materials, both single crystals and polycrystals [28].

$$v \propto \dot{\varepsilon}^{1/2} \tag{2}$$

Dominant frequency of AE signal is proportional to the velocity of dislocation [15]; hence, AE frequency should be proportional to the strain rate. This explains the shift of dominant frequency to higher value with increase in strain rate during yield region.

From Table 1, it is seen that a single AE dominant frequency in the range of 580–590 kHz and 710–730 kHz is generated during region 3 (during work hardening) and region 4 (UTS region) respectively. Dominant frequency generated in region 3 and region 4 does not vary with strain rate. Same dominant frequency shows that the AE source mechanism in these regions is not influenced by strain rate. When a material is work hardened, dislocation density increases and formation of new dislocations reduces the dislocation mean free path and hence, duration of AE event. Because of higher dislocation density in regions 3 and 4 [17], velocity effect of dislocation is not dominant with stain rate which explains same frequency range of AE spectra in these regions.

In necking region for all strain rate tests, lower dominant frequencies of almost the same order are observed. This is attributed to the crack growth whose mean lifetime is higher than dislocation related phenomenon [14]. AE spectral characteristics are directly connected to the nature of the mechanism and same dominant frequency generated during necking shows cracking behavior does not vary with strain rate.

3.2. *Infrared thermography*

Fig. 5 shows typical thermal images for different strain levels for $1.4 \times 10^{-2}\ s^{-1}$ strain rate. It can be seen that temperature of the gauge length increases with increase in nominal strain. Temperature increase is found to be highest at the center of the gauge length, where ultimately, necking occurs and fracture takes place. This clearly shows that thermography is capable of *a-priori* indicating the region of failure during

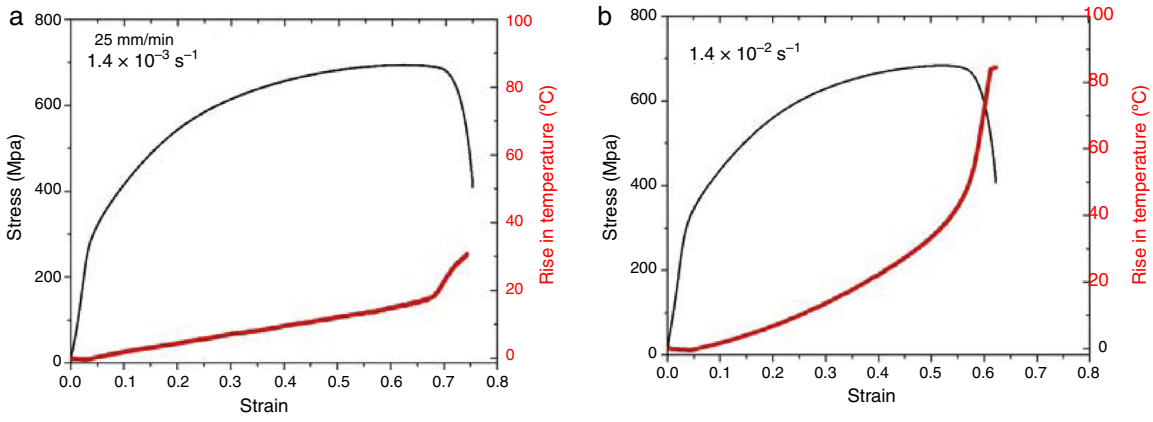

Fig. 6 – Variation of nominal stress and change in temperature with nominal strain for (a) 1.4 × 10^{-3} s^{-1} and (b) 1.4 × 10^{-2} s^{-1} strain rates.

deformation process. Similar results were obtained for other specimens and it was observed that temperature rise is higher for higher strain rates. During tensile testing the material undergoes progressive plastic deformation and nucleation of internal cavities occur which is followed by growth and subsequent coalescence of the cavities leading to failure [29,30]. During deformation, the stored plastic energy gets converted to heat energy and the specimen temperature increases. The temperature increase during necking is due to localized strain energy. Prior to fracture, void growth takes place and this is a function of strain and strain rate [29]. Moreover, it is reported that strain rate exponentially varies with tri-axial tension [29]. Hence, temperature rise during deformation is higher for higher strain rate.

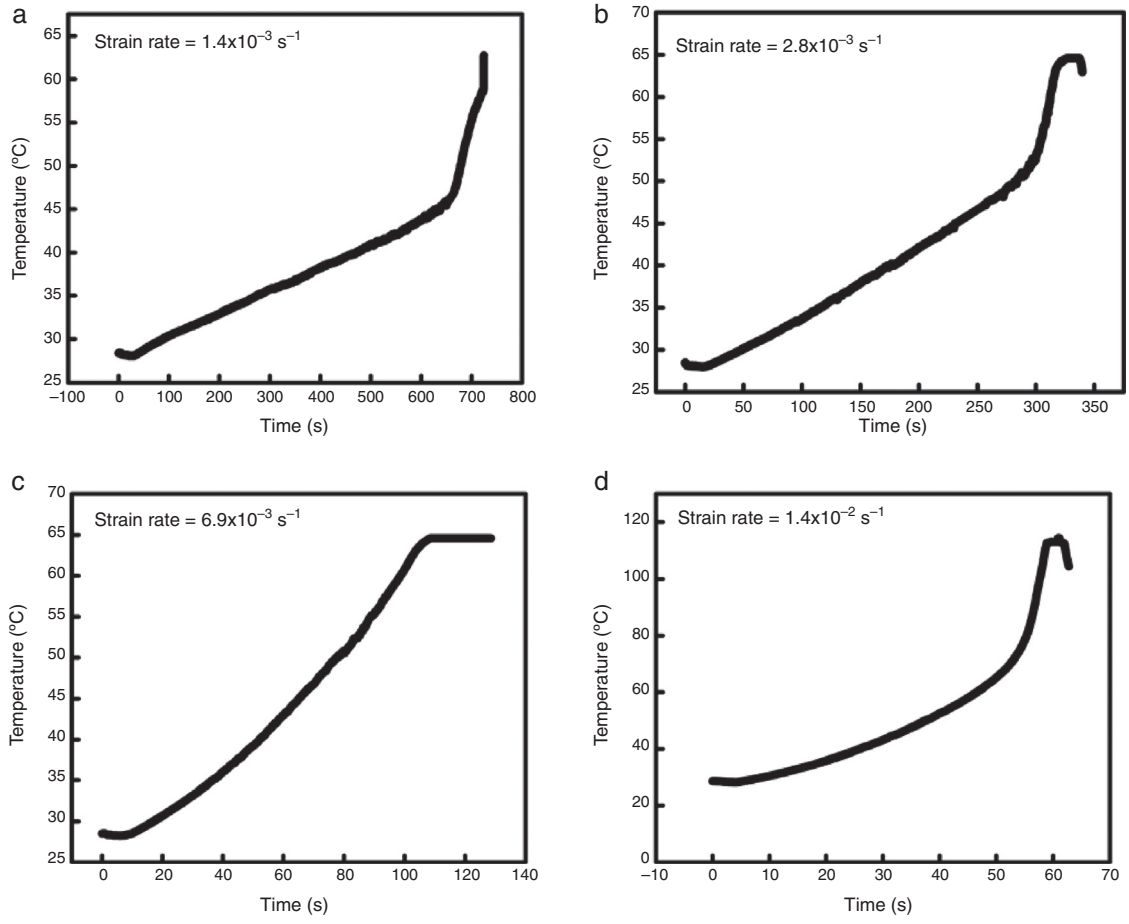

Fig. 7 – Variation of temperature with time during tensile deformation at the strain rates of (a) 1.4 × 10^{-3} s^{-1}, (b) 2.8 × 10^{-3} s^{-1}, (c) 6.9 × 10^{-3} s^{-1} and (d) 1.4 × 10^{-2} s^{-1}.

Table 2 – Average changes in temperature during different regions of deformation for different strain rates. The standard deviations (SD) in the measured temperature values are also shown.

Strain rate (s^{-1})	Change in temperature (Δt, °C) (±SD)			
	Region-1	Region-2	Region-3	Region-4
1.4×10^{-3}	−0.36 ± 0.01	0.9 ± 0.01	1 ± 0.02	13.5 ± 0.20
2.8×10^{-3}	−0.34 ± 0.01	1.1 ± 0.02	1.4 ± 0.03	17.5 ± 0.35
6.9×10^{-3}	−0.35 ± 0.01	1 ± 0.02	2.1 ± 0.03	20.5 ± 0.33
1.4×10^{-2}	−0.34 ± 0.01	1.2 ± 0.02	3.2 ± 0.06	51 ± 0.89

Variation of nominal stress and change in temperature (ΔT) with nominal strain for 1.4×10^{-3} and $1.4 \times 10^{-2}\ s^{-1}$ strain rates are shown in Fig. 6(a) and (b) respectively. Similar results were obtained for other strain rates. Temperature changes during different regions of deformation, i.e. (1) 0–3% nominal strain, (2) 3–10% nominal strain, (3) work hardening region and (4) around UTS to before final fracture have been monitored using IRT and shown in Table 2. Table 2 also shows the standard deviation (SD) of the measured temperature values over the regions of interest.

In region-1, a small drop in temperature (−0.36 ± 0.01 °C, −0.34 ± 0.01 °C, −0.35 ± 0.01 °C and −0.34 ± 0.01 °C for the strain rates of 1.4×10^{-3}, 2.8×10^{-3}, 6.9×10^{-3} and $1.4 \times 10^{-2}\ s^{-1}$, respectively) is observed for all strain rates (Table 2). In region-2, the values of temperatures changes are 0.9 ± 0.01 °C, 1.1 ± 0.02 °C, 1 ± 0.02 °C and 1.2 ± 0.02 °C for the four strain rates respectively. On the other hand, region-3 (work hardening) is characterized by steady rise in temperature with strain rate. For lower strain rate ($1.4 \times 10^{-3}\ s^{-1}$), there is a temperature rise of 1 ± 0.02 °C and for higher strain rate ($1.4 \times 10^{-2}\ s^{-1}$), the temperature rise is 3.2 ± 0.06 °C. In region-4 (UTS to final failure), considerable rise in temperature occurs and increases with strain rate. The temperature rise is 13.5 ± 0.20 °C for $1.4 \times 10^{-3}\ s^{-1}$ compared to 51 ± 0.89 °C for the higher strain rate of $1.4 \times 10^{-2}\ s^{-1}$.

The small temperature drop in the elastic region is due to thermoelastic effect, which occurs due to volume changes during elastic deformation [31]. Partial conversion of thermal energy to elastic energy results in the small magnitude of temperature drop [32]. The temperature drop observed in the present study is in close agreement with the reported values [33]. It is known that the temperature drop in 316 stainless steel due to thermoelastic effect decreases with increase in strain rate in the range 3.3×10^{-4} to $1.7 \times 10^{-3}\ s^{-1}$ [34]. In the present study, the magnitudes of temperature drop are 0.36 ± 0.01 °C, 0.34 ± 0.01 °C, 0.35 ± 0.01 °C and 0.34 ± 0.01 °C for the strain rates 1.4×10^{-3}, 2.8×10^{-3}, 6.9×10^{-3} and $1.4 \times 10^{-2}\ s^{-1}$, respectively. Though there is a small decrease in the magnitude of the temperature drop for higher strain rate, overall (incorporating the experimental and measurement accuracy) the temperature drop is found to be almost independent of the strain rate.

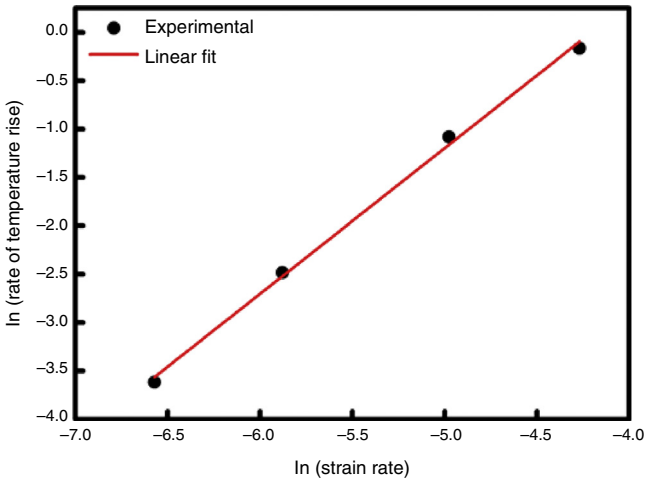

Fig. 8 – Variation of the logarithm of temperature rise rate ($\Delta T' = \Delta T/\Delta t$) as a function of logarithm of strain rate ($\dot{\varepsilon}'$).

In region-2, temperature increases steadily with deformation. The inversion in the temperature graph (decreasing trend in region-1 to increasing trend in region-2) is a clear indication of transition from elastic to plastic deformation in metallic materials [32]. The change in temperature rise is found to be independent of the strain rate. Nevertheless, it can be seen from Table 2 that there is a small increase in temperature rise with increasing strain rate.

In region-3, the work done is thermodynamically irreversible and it is reported that 95% of the total mechanical work gets converted to heat energy [34]. This causes the specimen temperature to increase continuously with progressive deformation, which is also evident from Table 2. With increasing strain rate, deformation progresses at an accelerated rate and the situation tends to be adiabatic.

Table 3 – Fit parameters for linear regression analyses of the temperature vs. time graphs in the work-hardening regions.

Strain rate (s^{-1})	Slope (°C s^{-1})	Intercept (°C)	Adjusted R^2
1.4×10^{-3}	0.0269 ± 8.52×10^{-6}	27.5166 ± 0.0033	0.9984
2.8×10^{-3}	0.08338 ± 6.32×10^{-5}	25.6617 ± 0.0106	0.9964
6.9×10^{-3}	0.33965 ± 7.56×10^{-4}	23.2272 ± 0.0422	0.9901
1.4×10^{-2}	0.84737 ± 0.00471	20.1422 ± 0.1527	0.9628

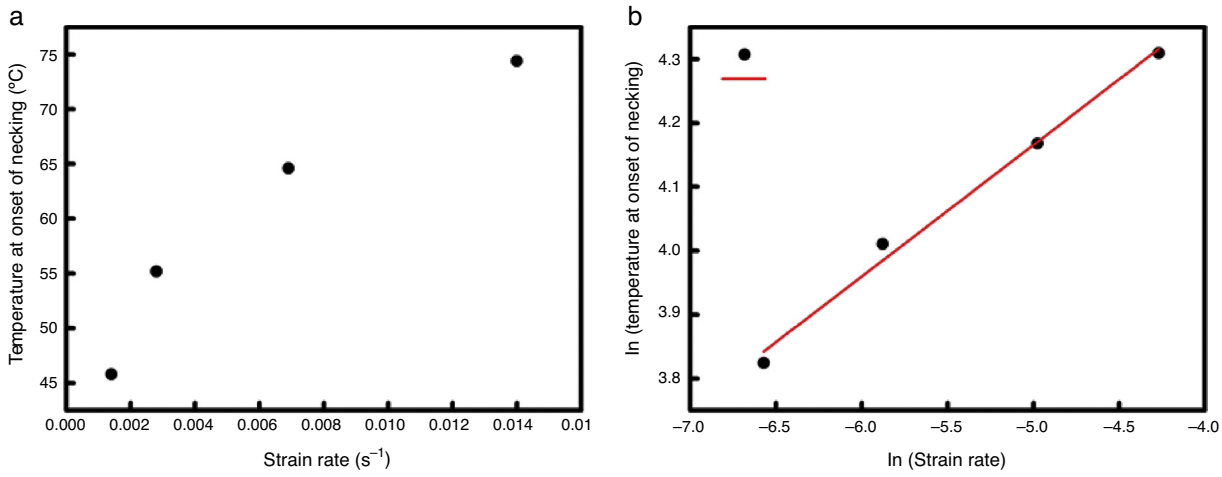

Fig. 9 – (a) Variation of temperature at the onset of necking with strain rate and (b) logarithm of necking temperature (T_n) with logarithm of the strain rate.

Under such conditions, the heat generation due to deformation is faster than the rate of heat diffusion throughout the specimen, which results in substantially larger temperature rise for higher strain rate experiments. Manifestation of this adiabatic heat generation is also higher during necking and fracture. Similar observations were reported earlier [34].

Fig. 7 shows the temperature increase as a function of time for all four strain rates. It can be seen from the figure that the temperature rise during tensile testing is in general a non-linear function of time. Nevertheless, the variation of temperature with time can be approximated as a linear function in the work-hardening region with good accuracy. The adjusted R^2 for the linear regression analyses of the temperature vs. time graphs are 0.9984, 0.9964, 0.9901 and 0.9628 for the strain rates of 1.4×10^{-3}, 2.8×10^{-3}, 6.9×10^{-3} and $1.4 \times 10^{-2}\,s^{-1}$, respectively. Table 3 shows the fit parameters in detail. The very high values of the coefficients of determination (nearly equal to 1) signify that the variation of temperature with time in the work hardening region can be approximated as a linear function of time with negligible errors. It can be further seen from the figure that the non-linear nature of the temperature vs. time curves increases with strain rate, which can be attributed to the increasing contribution from adiabatic heat generation for higher strain rates. This is also evident from the decreasing trend of the adjusted R^2 values of the linear regression analyses for higher strain rates. For $1.4 \times 10^{-2}\,s^{-1}$ strain rate, temperature rise in the work hardening region can be expressed by a non-linear equation of the form $T = a + bt^c$, where the constants a, b and exponent c are 29.66, 0.00984 and 2.1, respectively. The adjusted R^2 for this non-linear fit is 0.99, which reduces to 0.96 for linear approximation signifying the additional error involved in linear approximation as 3.03%, which is negligible. For the lower strain rates, the errors involved in linear approximation are much lower. The slopes of the linear regression analyses of the temperature vs. time graphs in the work hardening region provide the rate of temperature rise, which showed interesting correlation with the strain rates as subsequently discussed.

Fig. 8 shows the variation of logarithm of temperature rise rate ($\Delta T' = \Delta T/\Delta t$) in region-3 as a function of logarithm of strain rate (ε'). It can be seen that $\ln(\Delta T')$ increases linearly with $\ln(\varepsilon')$ with coefficient of determination (R^2) of 0.9967. The intercept and slope of the linear regression analysis are 6.33 ± 0.28 and 1.51 ± 0.05, respectively. Based on this observation the following equation is proposed:

$$\ln(\Delta T') = 7.25 + 1.69 \times \ln(\varepsilon') \quad (3)$$

It follows from Eq. (3) that the rate of temperature rise in region-3 (work hardening region) shows power law dependence with strain rate as shown in Eq. (4).

$$\Delta T' = 1408.105 \times (\varepsilon')^{1.69} \quad (4)$$

This equation shows that in region-3 thermal hardening of the material occurs. At higher strain rate, deformation induced heat generation occurs at a substantially higher rate than the rate of heat diffusion throughout the gauge length. Under such adiabatic conditions, rate of temperature increase is higher which is manifested by the empirical power-law equation.

Fig. 9(a) shows the variation of temperature at the onset of necking (T_n) with strain rate. It can be seen that T_n monotonically increases with strain rate. Fig. 9(b) shows the variation of ln (T_n) with ln (ε'). It can be seen that $\ln(T_n)$ linearly increases with $\ln(\varepsilon')$ with a coefficient of determination of 0.9881. The intercept and slope of the linear regression analysis are 5.19 ± 0.07 and 0.21 ± 0.01, respectively. From the above observation it can be stated that the variation of T_n with strain rate shows a power law dependence of the form $T_n = 179.47 \times (\varepsilon')^{0.21}$. For higher strain rates, localized deformation during necking adiabatically occurs at a higher rate which results in substantial increase in T_n, which follows the above power-law equation. The high thermal hardening coefficient in the work hardening region clearly shows that the rate of temperature increase is very sensitive to the strain rate of tensile deformation. Increase of necking temperature with strain

rate is thus due to the combined effect of localized deformation and strain rate induced adiabatic effects.

4. Conclusions

Acoustic emission and infrared thermography have been used to study tensile deformation of AISI type 316 stainless steel at different strain rates. Root mean square voltage of the AE signals generated increases with increase in strain rate and this is due to the increase in source activation. AE dominant frequency increased from elastic region to around 590 kHz during work hardening and 710 kHz around UTS for all strain rates. Shift in dominant frequency of AE to higher frequency with increase in strain is explained by reduced mean free path of dislocations. During necking, lower dominant frequencies are observed. AE dominant frequency increases with strain rate and this is attributed to the increase in the velocity of dislocations. The temperature increases steadily in the work hardening and necking regions. Magnitude of temperature rise increases with strain rate, which is due to higher rate of deformation induced heat generation compared to the rate of heat diffusion. An empirical equation relating the rate of temperature increase and strain rate is proposed. This study shows that complementary NDE techniques like AE and IRT can be used for online monitoring and characterization of tensile deformation. Studies on materials like 2.25 Cr-1 Mo steel and low carbon steel with elaborate yield point would be taken up to understand effect of strain rate on AE dominant frequency and temperature rise rate during different regions of deformation.

Conflicts of interest

The authors declare no conflicts of interest.

Acknowledgement

Authors are thankful to Dr. P.R. Vasudeva Rao, Director, IGCAR, Kalpakkam for constant encouragement and support.

REFERENCES

[1] Mukhopadhyay CK, Haneef TK, Rao BPC, Jayakumar T. Condition monitoring of exchange towers of heavy water plant during hydrotesting by acoustic emission technique. Insight 2011;53:29–33.
[2] Bagavathiappan S, Lahiri BB, Saravanan T, Philip J, Jayakumar T. Infrared thermography for condition monitoring – a review. Infrared Phys Technol 2013;60:35–55.
[3] Kordatos EZ, Aggelis DG, Matikas TE. Monitoring mechanical damage in structural materials using complimentary NDE techniques based on thermography and acoustic emission. Compos B: Eng 2012;43:2676–86.
[4] Miller RK, Mclntire P. Acoustic emission testing: nondestructive testing hand book, 3rd ed. Columbus, OH, USA: American Society for Nondestructive Testing; 2005.
[5] Kiesewetter N, Schiller P. The acoustic emission from moving dislocations in aluminium. Phys Status Solidi A 1976;38:569–76.
[6] Fleischmann P, Lakestani F, Baboux JC, Rouby D. Spectral and energy analysis of a moving ultrasonic source-application of acoustic emission to aluminium during plastic deformation. Mater Sci Eng 1977;29:205–12.
[7] Wadley HNG, Scruby CB. Cooling rate effects on acoustic emission-microstructure relationships in ferritic steels. Mater Sci Eng 1991;26:5777–92.
[8] Carpenter SH, Pfleiderer C. Acoustic emission from AISI 4340 steel as a function of strength. J Acoust Emiss 1994;12:141–8.
[9] Khamedi R, Fallahi A, Oskouei AR. Effect of martensite phase volume fraction on acoustic emission signals using wavelet packet analysis during tensile loading of dual phase steels. Mater Des 2010;31:2752–9.
[10] Haneef TK, Mukhopadhyay CK, Rao BPC, Jayakumar T. Acoustic emissions generated during Lüders band elongation of tempered medium carbon steel. Strength Fract Complex 2010;6:149–59.
[11] Barat K, Bar HN, Mandal D, Roy H, Sivaprasad S, Tarafder S. Low temperature tensile deformation and acoustic emission signal characteristics of AISI 304LN stainless steel. Mater Sci Eng A 2014;597:37–45.
[12] Raj B, Jayakumar T. Acoustic emission: current practices and future directions. ASTM STP 1077. Philadelphia, PA: American Society for Testing and Materials; 1990. p. 218–41.
[13] Raj B, Jayakumar T. Acoustic emission during tensile deformation in austenitic stainless steel. J Acoust Emiss 1989;8:S26.
[14] Raj B, Jha BB, Rodriguez P. Frequency spectrum analysis of acoustic emission signal obtained during tensile deformation and fracture of an AISI 316 type stainless steel. Acta Metal 1989;37:2211–5.
[15] Moorthy V, Jayakumar T, Raj B. Acoustic emission technique for detecting micro- and macroyielding in solution-annealed AISI Type 316 austenitic stainless steel. Int J Press Vessel Pip 1995;44:161–8.
[16] Pattnaik AB, Jha BB, Sahoo R. Effect of strain rate on acoustic emission during tensile deformation of α-brass. Mater Sci Technol 2013;29:294–9.
[17] Zhiyuan H, Hongyun L, Hongwei W. Effects of strain rate and notch on acoustic emission during the tensile deformation of a discontinuous yielding material. Mater Sci Eng A 2011;528:4372–80.
[18] Venkataraman B, Mukhopadhyay CK, Raj B. Effect of variation of strain rate on thermal and acoustic emission during tensile deformation of nuclear grade AISI type 316 stainless steel. Mater Sci Technol 2004;20:1310–6.
[19] Maldague X. Theory and practice of infrared technology for nondestructive testing, 1st ed. Dallas, TX, USA: Wiley Interscience; 2001.
[20] Meola C, Carlomagno GM, Giorleo L. The use of infrared thermography for materials characterization. J Mater Process Technol 2004;155–156:1132–7.
[21] Wong BS, Tui CG, Bai W, Tan BH, Low BS, Tan KS. Thermographic evaluation of defects in composite materials. Insight 1999;41:504–9.
[22] Lahiri BB, Bagavathiappan S, Saravanan T, Rajkumar KV, Kumar A, Philip J, et al. Defect detection in weld joints by infrared thermography. In: Proceedings of the international conference on NDE in steel and allied industries. 2011. p. 191–7.
[23] Mukhopadhyay CK, Ray KK, Jayakumar T, Raj B. Acoustic emission from tensile deformation of unnotched and notched specimens of AISI type 304 stainless steels. Mater Sci Eng A 1998;255:98–106.
[24] Magnani FS, da Silva RNT. Infrared thermography applied to the quantitative determination of spatial and thermophysical parameters of hidden included objects. Appl Therm Eng 2007;27:2378–84.

[25] Lahiri BB, Bagavathiappan S, Soumya C, Mahendran V, Pillai VPM, Philip J, et al. Infrared thermography based defect detection in ferromagnetic specimens using a low frequency alternating magnetic field. Infrared Phys Technol 2014;64:125–33.
[26] Imeda H, Kuganagi K, Kimura H, Nakasa H. Proceedings of the third acoustic emission symposium. 1976. p. 492.
[27] Heiple CR, Carpenter SH. Acoustic emission produced by deformation of metals and alloys – a review: Part II. J Acoust Emiss 1987;6:215–37.
[28] Heiple CR, Carpenter SH. Acoustic emission produced by deformation of metals and alloys – a review: Part I. J Acoust Emiss 1987;6:177–205.
[29] Venkatraman B, Mukhophadyay CK, Raj B. Prediction of tensile failure of 316 stainless steel using infrared thermography. Exp Tech 2004;28:35–8.
[30] Vanstone RH, Cox TB, Low JR, Psioda JA. Microstructural aspects of fracture by dimpled rupture. Int Met Rev 1985;30:157–79.
[31] Jalaj K, Baby S, Vikas K. Thermographic studies on IMI-834 titanium alloy during tensile loading. Mater Sci Eng A 2008;496:303–7.
[32] Ferron G. The effect of the interruption of straining on non-uniform plastic flow in tension. Mater Sci Eng 1982;52:133–8.
[33] Elzbieta P. Thermoelastic effect in austenitic steel referred to its hardening. J Theor Appl Mech 1999;2:349–68.
[34] Venkataraman B, Raj B, Mukhopadhyay CK, Jayakumar T. Correlation of infrared thermographic patterns and acoustic emission signals with tensile deformation and fracture processes. Rev Prog Quant Nondestr Eval 2001;20: 1443–50.